Counterdirectional mode coupling in ring resonators with QPM nonlinear crystals and effects on the characteristics of cw optical parametric oscillation

**S. Vasilyev · H.-E. Gollnick · A. Nevsky · A. Grisard ·
E. Lallier · B. Gérard · J. Jimenez · S. Schiller**

Abstract The effects of coupling between clockwise and counterclockwise modes in ring resonators due to back reflections from QPM gratings in nonlinear crystals are investigated. We demonstrate, using simulations, that the non-phase-matched back reflection due to typical imperfections of the QPM grating has a relevant magnitude and can give rise to the coupling. We developed an analytical model and evaluated parameters of a singly resonant OPO in the presence of this coupling, which indicates that the threshold pump power is doubled in the limit of strong coupling. We also evaluated the effect of the coupling with respect to resonant power enhancement for cavity-enhanced nonlinear frequency mixing applications, finding that the enhancement is reduced by up to a factor four. Experimental observations based on PPLN and orientation-patterned GaAs crystals and model predictions are in good agreement. We propose and demonstrate a method for active stabilization of ring resonators with mode coupling that relies on the dissimilarity of the coupled forward and backward modes.

S. Vasilyev (✉) · H.-E. Gollnick · A. Nevsky · S. Schiller
Institut für Experimentalphysik, Universitätsstr. 1,
40225 Düsseldorf, Germany
e-mail: sergey.vasilyev@uni-duesseldorf.de

A. Grisard · E. Lallier
Thales Research and Technology, RD 128, 91767 Palaiseau
Cedex, France

B. Gérard
Alcatel-Thales III–V Lab, RD 128, 91767 Palaiseau Cedex,
France

J. Jimenez
Física de la Materia Condensada, Universidad de Valladolid,
47011 Valladolid, Spain

1 Introduction

The effects of counterdirectional mode coupling in ring laser resonators attracted attention shortly after the advent of lasers, in connection with the development of laser gyroscopes [1]. More recently the interest has been centered on the investigation of the counterdirectional mode coupling in high-finesse monolithic traveling-wave microresonators in the form of rings, disks and spheres [2–8]. Clockwise and counterclockwise modes in those resonators are coupled due to the backscattering on residual inhomogeneities, distributed in the resonator matrix and due to surface roughness. It was demonstrated that the coupling in the microresonator could be induced or modified by a subwavelength tip without degrading the Q factor of the resonator [6, 7]. The coupling can also be introduced by a nanometer-scale grating along the sidewalls of the ring cavity [8].

The counterdirectional mode coupling destroys the directionality of a traveling-wave resonator and its impedance matching. Besides, the coupling causes splitting of the resonant peaks due to lifting of the degeneracy of two counter propagating modes.

In this paper, we investigate effects of the counterdirectional mode coupling in ring resonators with quasi-phase-matched (QPM) nonlinear crystals for applications such as cavity-enhanced nonlinear frequency mixing and optical parametric oscillation. Two types of QPM materials were characterized: a commercial periodically poled magnesium doped lithium niobate (PPLN) crystal, and an orientation-patterned gallium arsenide (OP-GaAs) crystal, a new nonlinear material for mid-IR frequency conversion applications [9–11]. According to our observations, the effects of counterdirectional mode coupling can be rather pronounced in low-finesse (10^2–10^3) ring resonators containing those crystals. We show that in this case an important contribution to

the coupling is the back reflection from the crystal's QPM grating.

In Sect. 2 we evaluate numerically the back-reflection strength from a QPM crystal. In Sect. 3 we compare the amplitudes of clockwise and counterclockwise modes in the ring cavity in two regimes. In the passive regime the cavity resonates the external optical wave and in the active regime the cavity resonates the signal wave of the optical parametric oscillator. We evaluate theoretically limitations on performance of the cavity due to counterdirectional mode coupling in both regimes. Then, we show that the disparity of resonances in two opposite directions can be used for active stabilization of the cavity. In Sect. 4 we compare predictions of the model with our experimental observations.

2 Evaluation of the back reflection from a QPM crystal

Strong back reflection from a QPM crystal can be explained by the following consideration: (i) the incoming electromagnetic wave is partly scattered on inhomogeneities, located at equidistant domain interfaces in the QPM crystal; (ii) the back reflection is poorly phase matched since the QPM grating is not specially designed to be a Bragg reflector for the incoming wave; (iii) nevertheless, a non-phase-matched back reflection may build-up to a considerable level due to domain-to-domain fluctuations of QPM crystal properties.

In order to evaluate the back-reflection coefficient of the QPM grating we performed a computer simulation. Our code for rigorous modeling of diffraction gratings [12, 13] was adapted to compute the zero-order reflection of a plane wave from a multilayer stack with a finite number of layers. A simplified model of the QPM crystal was used for the simulations. We assume that the crystal's domains have a constant refractive index n_0 and are separated by domain interfaces with thicknesses δ_i and perturbed refractive indexes n'_i where i is the domain number.

Simulations were carried out using parameters of the OP-GaAs crystal. The cathodoluminescence (CL) technique was used to characterize the OP-GaAs samples [14]. A CL image of a cleaved OP-GaAs crystal is shown in Fig. 1. Domains with inverted crystallographic orientation, (001) and (00-1), can be recognized in the CL image due to different contrast.
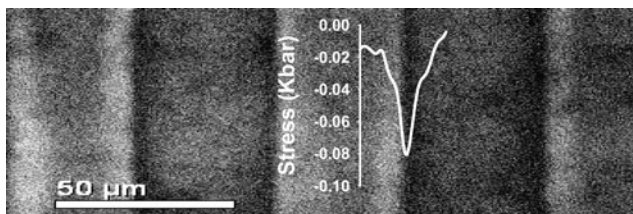

Fig. 1 Cathodoluminescence image of the OP-GaAs crystal and the stress distribution around the domain interface (*white*)

CL experiments revealed perturbed areas between the adjacent domains. The refractive index at the domain interface is perturbed due to the concentration of defects, and the mechanical stress induced by those defects. The white curve in Fig. 1 shows the stress distribution at the domain interface obtained from CL measurements. The refractive index in the domain interface can be approximated as $n' = n_0(1 + \kappa)$ with the contrast of the QPM grating $\kappa \simeq 4 \times 10^{-4}$ deduced from the average stress at the interface [15]. The typical thickness of the domain interface δ in OP GaAs samples is 6–10 μm. Standard deviations $\sigma(\kappa)$ and $\sigma(\delta)$ were estimated as 5–10% of the respective mean values $\bar{\kappa}$ and $\bar{\delta}$, based on the CL contrast images. The 10-mm long OP-GaAs crystal with the QPM grating period $\Lambda = 50$ μm was approximated by a 800-layer stack (two domains and two interfaces per period).

The calculated reflection coefficient from the perfectly periodic structure ($\kappa_i = 4 \times 10^{-3}, \delta_i = 10^{-1}\Lambda$) as a function of the incident wavelength $\lambda \approx 2000$ nm is shown in Fig. 2 by the black line. Two peaks in the spectrum correspond to the usual Bragg reflection. The reflection coefficient rapidly drops to the 10^{-7} level if the wavelength is detuned from the Bragg resonance.

In the next simulation we have introduced random fluctuations to the parameters κ_i and δ_i. The reflectance spectrum of the QPM grating in presence of 5% fluctuations ($\sigma(\kappa)/\bar{\kappa} = \sigma(\delta)/\bar{\delta} = 0.05$) is shown in Fig. 2 by the red
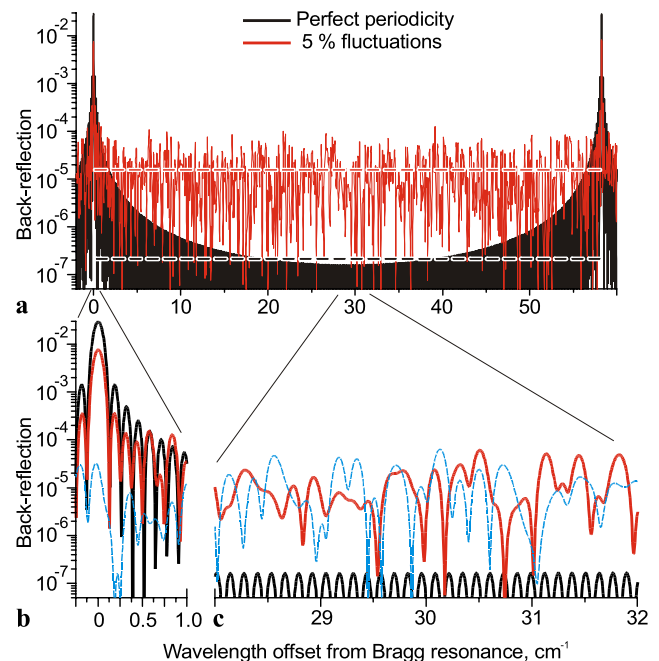
Fig. 2 Simulated power reflection coefficient R_b of the QPM grating vs. wavelength. *Black*: perfectly periodic grating, *red*: grating with random fluctuations, *dotted horizontal lines*: averaged reflection coefficients (geometric mean). *Blue dotted line* in parts (**b**) and (**c**): 'zero contrast' QPM grating ($\kappa = 0, \sigma(n')/\bar{n}' = 4 \times 10^{-4}$)

line. Part (b) of the figure shows the vicinity of the Bragg resonance and part (c) shows the off-resonance part of the spectrum in more detail. As can be seen, fluctuations of the grating parameters result in some decrease of the phase-matched Bragg reflection. On the other hand, the non-phase-matched back reflection builds up and can be considerably higher than the non-phase-matched reflectance of the perfectly periodic grating. The reflectance of the QPM grating is sensitive to small changes of the radiation wavelength and its dependence on the wavelength is rather irregular.

For further evaluations we considered the averaged reflectance of the QPM grating. Averaging was carried out over the whole spectral interval between the adjacent Bragg resonances. We used averaging in terms of the geometric mean, since the dependence of the reflectance on the wavelength is very strong. The averaged reflectance of perfectly periodic and perturbed gratings are shown in Fig. 2(a) by dotted horizontal lines.

The dependence of the averaged reflectance of the QPM grating on the level of fluctuations is shown in Fig. 3. Simulations were carried out for the contrast of the grating $\bar{\kappa} = 4 \times 10^{-4}$ (a typical value for the OP-GaAs crystal) and for a twice-higher contrast, for comparison. As can be seen, the increase of fluctuations to from the 0.1% to the 1–2% level results in increase of averaged reflectance by two orders of magnitude (whereas the peak values of the non-phase-matched reflectance can be three orders of magnitude higher than those of the perfectly periodic structure). On the other hand, our simulation shows a saturation effect: fluctuations above 2–3% do not result in a further increase of the back reflection from the QPM grating. Furthermore, Fig. 3 illustrates a quadratic dependence of the reflectance on the grating contrast κ.

Another interesting effect due to a non-perfect periodicity of the QPM grating is the build-up of back-reflection from a structure with a 'zero contrast' ($\bar{\kappa} = 0$). In such a structure the mean value of the refractive index in the domain interface equals the index of the bulk material ($\bar{n}' = n_0$)

and the refractive indexes at the individual interfaces fluctuate symmetrically with respect to n_0. The reflectance of the 'zero contrast' grating is illustrated in Fig. 2 by the blue dotted line. The fluctuations of the refractive index in the domain interfaces $\sigma(n')/\bar{n}' = 4 \times 10^{-4}$ were set to be the same as the contrast κ of the grating in our previous simulations. The 'zero contrast' grating has no Bragg resonances in the reflectance spectrum. However, the non-phase-matched reflectance is at the same level as for the grating with the contrast $\bar{\kappa} = 4 \times 10^{-4}$ and with $\sigma(\kappa)/\bar{\kappa} = 5\%$ fluctuations.

The presented results are qualitative, as we did not take into account the diffraction of the incoming wave on the QPM grating itself (dozens of diffraction orders must appear since $\lambda \ll \Lambda$), nor the effects due to the beam focusing inside the crystal. Besides, crystallographic planes of the two domain orientations in the OP-GaAs crystal could be slightly tilted (1–3°). Such a misorientation of domains could also affect the back reflection from the OP-GaAs crystal. Nevertheless, we can make two important conclusions: (i) the back reflection from the QPM crystal can be counter-intuitively strong due to fluctuations of the QPM grating parameters; (ii) the back reflection is hardly controllable due to its sensitivity to the wavelength and the QPM grating period (which itself depends on the crystal's temperature). Furthermore, the back-reflection measurement can be used as a tool for characterization of QPM crystals.

3 Model of the ring resonator with QPM crystal

3.1 Passive cavity

A schematic of a ring cavity with a QPM crystal is shown in Fig. 4. Without loss of generality, we assume that the cavity consists of two mirrors with respective reflectivities R_1 and R_2 and that the QPM crystal serves as the third mirror. All dissipation losses are incorporated into the model via the power loss factor $V = v^2$ of the crystal. Besides, the
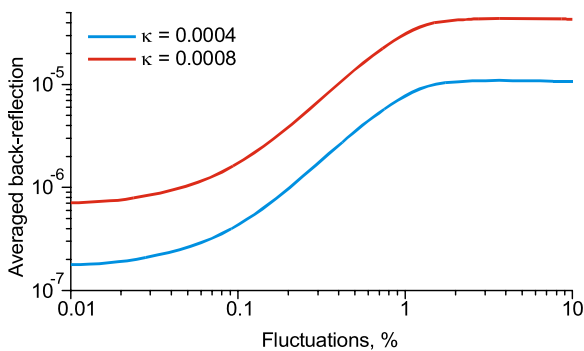
Fig. 3 Averaged (geometric mean) reflection coefficient of the QPM grating vs. fluctuations $\sigma(\kappa)/\bar{\kappa} = \sigma(\delta)/\bar{\delta}$ of the grating parameters. *Blue*: the grating contrast $\bar{\kappa} = 4 \times 10^{-4}$, *red*: $\bar{\kappa} = 8 \times 10^{-4}$
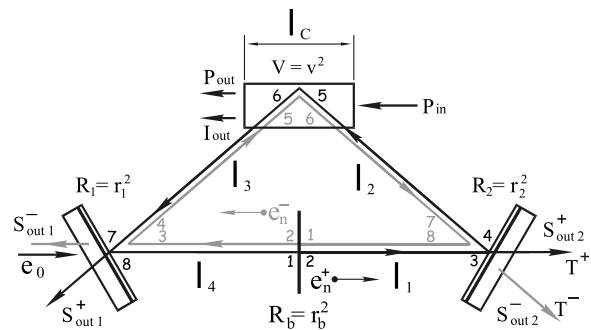
Fig. 4 Schematic of the ring cavity with the QPM crystal. In 'passive' regime the cavity resonates the external wave with the amplitude e_0. In 'active' regime the cavity resonates the signal wave of the SRO. See text for other notations

crystal has a backward reflection R_b through which the two counter-propagating modes are coupled. For simplicity of analysis, we locate the source of backward reflection not inside the crystal, but in an infinitesimally thin region between two mirrors (black vertical line in Fig. 4).

In the passive regime the cavity resonates the external electromagnetic wave that is coupled into the cavity via the left mirror. The 'e$_0$' arrow in Fig. 4 denotes the incoming wave and the $T^{\pm}$ arrows show the cavity transmission via the second mirror in forward (counterclockwise) and backward directions. The loop equations for the passive cavity can be written as follows [3]:

$$
\begin{aligned}
e_2^+ &= t_b e_1^+ + i r_b e_1^-, & e_3^+ &= \exp(ikl_1)e_2^+, \\
e_4^+ &= r_2 e_3^+, & e_5^+ &= \exp(ikl_2)e_4^+, \\
e_6^+ &= v e_5^+, & e_7^+ &= \exp(ikl_3)e_6^+, \\
e_8^+ &= r_1 e_7^+ + t_1 e_0^+, & e_1^+ &= \exp(ikl_4)e_8^+,
\end{aligned}
\tag{1a}
$$

$$
\begin{aligned}
e_2^- &= t_b e_1^- + i r_b e_1^+, & e_3^- &= \exp(ikl_4)e_2^-, \\
e_4^- &= r_1 e_3^-, & e_5^- &= \exp(ikl_3)e_4^-, \\
e_6^- &= v e_5^-, & e_7^- &= \exp(ikl_2)e_6^-, \\
e_8^- &= r_2 e_7^-, & e_1^- &= \exp(ikl_1)e_8^-,
\end{aligned}
\tag{1b}
$$

$$
e_T^+ = -t_2 e_3^+, \qquad e_T^- = -t_2 e_7^-
\tag{1c}
$$

where $e_i^{\pm}$ are the wave amplitudes in forward and backward directions (note that the reference points of forward and backward wave for a given index do not coincide); l_i are optical path lengths from one reference plane to another ($\Sigma l_i = L$, the cavity length); t_1, t_2 are mirrors' amplitude transmission coefficients; v is the amplitude loss factor; $t_b = \sqrt{1 - R_b}$ is the amplitude transmission factor associated with the coupling; k is the propagation constant; and e_0 is the amplitude of the incoming wave. From (1) one can determine the fractions of the incident wave intensity ($\sim |e_0|^2$) being transmitted by the cavity in forward and backward directions:

$$
\begin{aligned}
T^+ &= \frac{(1-R_1)(1-R_2)((t_b-\rho)^2 + 4s^2\rho t_b)}{((t_b-\rho)^2 + 4s^2\rho t_b + R_b)^2 + 16s^2(s^2-1)\rho^2 R_b}, \\
T^- &= \frac{(1-R_1)(1-R_2)V R_1 R_b}{((t_b-\rho)^2 + 4s^2\rho t_b + R_b)^2 + 16s^2(s^2-1)\rho^2 R_b}
\end{aligned}
\tag{2}
$$

where $\rho = \sqrt{R_1 R_2 V}$ and $s = \sin(kL/2)$. Equations (2) reveal two features of the cavity with counterdirectional mode coupling: (i) for each output direction, the resonances (maxima of transmitted power vs. frequency $\omega = ck$) are split; (ii) the shape of resonances and the frequencies of resonance maxima are not the same for two opposite directions. The effect of splitting is discussed in detail e.g. in [2–5, 7, 8]. Here

we focus our attention on the dissimilarity of the cavity resonant properties in forward and backward directions.

Evaluation of (2) is simple if both the cavity round-trip loss $\alpha = 1 - R_1 R_2 V$ and the coupling constant R_b are small. The magnitude of resonance splitting for forward mode (σ) can be approximated as $\sigma \simeq \sqrt{R_b}/\pi$, while the width of the resonance peak (Δ) is given by $\Delta = \alpha/2\pi$. Hence, the cavity can be characterized using their ratio, or the parameter

$$
\chi = \sqrt{R_b}/\alpha.
\tag{3}
$$

Cavity transmissions, calculated using (2), for different values of the parameter χ are illustrated in Fig. 5. Calculations were made for $R_1 = R_2 = \sqrt{1-\alpha}$ and $V = 1$. Three coupling regimes can be distinguished. (a) Strong coupling ($\chi \gg 1$): the magnitude of peak splitting σ is much higher than the width of the resonance; forward and backward resonances have similar shape. (b) Intermediate regime ($\chi \approx 1$): the peak splitting is of the same order as the width of the resonance and shapes of forward and backward resonances are distinctly different. (c) Weak coupling ($\chi \ll 1$): the peak splitting is absent in backward direction and the forward resonance is rather flattened than split. With further decrease of the constant χ the resonance peak in forward direction tends to the Lorentz profile, while the backward transmission tends to zero.

The positions of the cavity transmission maxima in forward and backward directions do not coincide and the offset
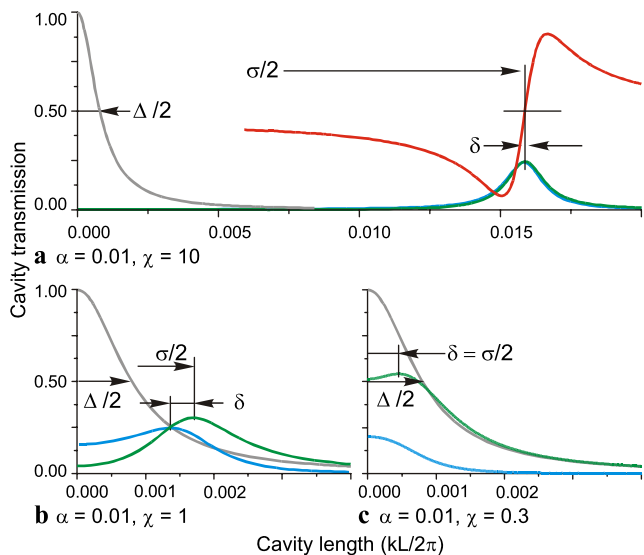

Fig. 5 Transmission resonances of the ring cavity with counterdirectional mode coupling for different values of the parameter χ: *green curves* forward transmission T^+; *blue curves* backward transmission T^-; *grey curves* transmission of the cavity in the absence of the coupling; *red curve* the $\delta T = T^+ - T^-$ signal (in different vertical scale). The figure shows halves of the split resonance peaks and the second halves are symmetrical with respect to the vertical axes. Horizontal axes are normalized to the free spectral range of the cavity and vertical axes are normalized to the incoming wave intensity

between them can be approximated as:

$$\delta \simeq \frac{\Delta}{2}\chi\left(\sqrt{1+\frac{1}{\chi^2}}-1\right). \qquad (4)$$

The offset δ is small in comparison with the width of the resonance Δ in the strong coupling regime ($\chi \gg 1$). The difference $\delta T = T^+ - T^-$ of the cavity transmissions in forward and backward directions exhibits a dispersive shape versus frequency, which can be used as an error signal for active stabilization (see Sect. 4.1). The δT signal is shown in Fig. 5(a) by red line (with different vertical scale). The zero crossing of the signal is located in vicinity of the transmission maximum and can be fine tuned by producing a weighted difference of T^+ and T^-. The zero crossing shifts with respect to the transmission maxima if the parameter χ changes. However, this shift is small in the strong coupling regime. The intermediate regime is less favorable for active stabilization of the cavity due to a stronger dependence of the zero crossing position on the parameter χ.

Figure 6 illustrates the effects of the counterdirectional mode coupling on the ability of the cavity to enhance the intensity of the incoming wave. The figure shows the dependence of the cavity transmission at resonance in forward direction, a measure of the power circulating in forward direction, on the transmission of the input mirror $(1 - R_1)$. To make the figure more illustrative, the horizontal axis was normalized to the transmission of the output mirror and other losses were zeroed ($V = 1$). The black curve corresponds to the cavity without the coupling and illustrates the familiar rule for the cavity impedance matching: all incoming wave is coupled to the cavity and hence the intracavity intensity is highest if transmission of the input mirror equals all other losses (the output mirror transmission, in this case).
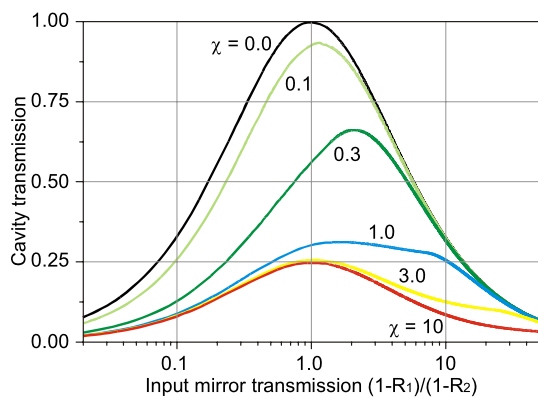
Fig. 6 Cavity transmission at resonance in forward direction vs. input mirror transmission. *Black curve*: transmission of the cavity in the absence of the coupling; *color curves*: transmission of the cavity for different values of the parameter χ. Horizontal axis is normalized to the to the transmission of the output mirror and vertical axis is normalized to the incoming wave intensity

The colored curves allow estimating the impedance matching of the cavity for different regimes of the counterdirectional mode coupling. As can be seen, the maximum intracavity intensity decreases monotonically with increasing χ. The optimal transmission of the input mirror depends on the coupling regime. The effects of the coupling can be partly compensated in the weak coupling regime by increasing the input mirror transmission e.g. by a factor of two at $\chi = 0.3$ (green curve). The optimal transmission is rather uncritical in the intermediate regime: a fivefold variation of the transmission results in a change of the intracavity intensity by 7% at $\chi = 1$ (blue curve). The shape of the curve and the optimal condition in the strong coupling regime ($\chi = 10$, red curve) are the same as for the cavity without the coupling (black curve). However, only a quarter of the incoming intensity can be coupled into the forward mode, another quarter is coupled to the backward mode and the rest is reflected as well as back-reflected from the input mirror.

3.2 Active cavity

A common use of a ring cavity with a QPM crystal is as an optical parametric oscillator (OPO). The crystal is pumped at the wavelength $\lambda^{(P)}$ with pump intensity P_{in} (see Fig. 4). Parametric interaction results in amplification of the signal wave $\lambda^{(S)}$ and generation of the idler wave at the wavelength $1/\lambda^{(I)} = 1/\lambda^{(P)} - 1/\lambda^{(S)}$ with intensity I_{out}. The pump wave is depleted: $P_{\text{out}} < P_{\text{in}}$. In the simplest case of the singly resonant OPO (SRO) the cavity resonates only the signal wave while the pump and the idler waves make a single pass through the crystal. Besides, one can assume that amplification of the signal occurs only in forward direction since the phase mismatch between the backward wave at signal wavelength and the pump is typically very large. Hence, the loop equations for the SRO signal wave amplitudes are similar to (1) for the passive cavity. The differences between (1a) and the equations for the SRO signal in forward direction are the following:

$$e_8^+ = r_1 e_7^+ + t_1 e_0 \rightarrow e_8^+ = r_1 e_7^+,$$

$$e_6^+ = v e_5^+ \rightarrow e_6^+ = v e_5^+ + v e_G^+. \qquad (5)$$

Here the incoming wave e_0 is zeroed and the term e_G^+ is introduced instead, to take into account a net addition to the signal wave due to the parametric interaction. The equations for the backward wave and for the output signal wave amplitudes are the same as (1b) and (1c).

The signal wave amplitude e_5^+ is infinitesimally small at the SRO threshold and the parametric interaction can be considered analytically in the low pump depletion approximation:

$$g = 1 + e_G^+/e_5^+ = \cosh(\Gamma l_C) \simeq 1 + \Gamma^2 l_C^2/2. \qquad (6)$$

Here the factor g is the ratio of the signal amplitude at the output of the crystal to the input signal and l_C is the length of the crystal. For interaction of focused Gaussian beams the parametric gain Γ can be approximated as [16]:

$$\Gamma^2 = \frac{16\pi^2 d_{\text{eff}}^2}{c\varepsilon_0 n_p n_s n_i} \frac{\lambda_p^2}{\lambda_s^2 \lambda_i^2} \frac{\bar{h}_m(\xi)}{\xi} P_{\text{th}},$$

$$\xi = \frac{l_C}{b}, b = \frac{2\pi n w_0^2}{\lambda}, \tag{7}$$

where P_{th} is the pump intensity at the SRO threshold and the maximum value of the focusing function $\bar{h}_m(\xi) \simeq 1$ is reached for a beam focusing parameter $\xi \simeq 2.8$. Equations (1), (5) and (6) result in the following expression for the steady-state parametric gain of the SRO at threshold:

$$\left(\frac{1}{2}\Gamma^2 l_C^2\right)^2$$

$$= \frac{1}{\rho^2} \frac{((t_b - \rho)^2 + 4s^2\rho t_b + R_b)^2 + 16s^2(s^2-1)\rho^2 R_b}{(t_b - \rho)^2 + 4s^2\rho t_b}$$

$$\propto \frac{1}{T^+}. \tag{8}$$

As can be seen, the parametric gain at threshold is inversely proportional to the forward transmission of the passive cavity, see (2). This similarity allows us to use the results obtained above for the passive cavity for analysis of the active SRO cavity.

The SRO oscillation occurs for that parameter value $s = \sin(kL/2)$ (i.e. at the signal wavelength) that corresponds to the smallest gain (e.g at the minimum of the curve defined by (8)). The counterdirectional mode coupling results in a splitting of the curve's minima, similar to the splitting of the resonance maxima in the passive cavity. Thus, the SRO may oscillate at either of two frequencies symmetrically shifted from the "central" frequency of the cavity. Besides, the coupling results in an increase of the SRO threshold, in the same way as it decreases the peak transmission of the passive cavity (see Fig. 5 and Fig. 6). Another probable effect, which remains to be studied, is hopping of the SRO's signal frequency between the two halves of the split resonance.

Figure 7 shows the dependence of the SRO threshold P_{th} on the parameter $\chi = \sqrt{R_b}/\alpha$ computed from (8). The threshold is shown normalized to that in the absence of coupling ($\chi = 0$). A simple rule of thumb can be used to evaluate the influence of the counterdirectional mode coupling on the SRO threshold: in the weak coupling regime ($\chi \ll 1$) the threshold is almost not affected; in the strong coupling regime ($\chi \gg 1$) the threshold is twice higher than that in the absence of coupling; in the intermediate regime the threshold strongly depends on the exact value of the parameter χ.

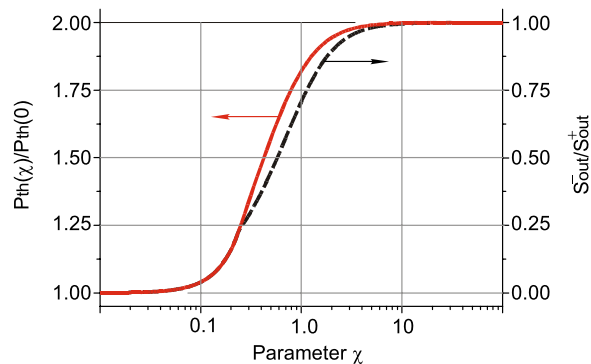The increase of the SRO threshold in presence of the counterdirectional mode coupling can be explained by the

Fig. 7 SRO threshold (*red curve*) and ratio between signal output intensity in backward and forward directions (*black dashed curve*) vs. the parameter χ. Left vertical axis is normalized to the SRO threshold in the absence of coupling ($\chi = 0$)

following qualitative consideration: (i) a part of the generated signal photons is coupled to the counter-propagating mode and does not interact with the pump; (ii) this can be interpreted as a decrease of the effective parametric gain in the QPM crystal; (iii) hence, the pump power must be proportionally increased to reach the SRO threshold. Half of the signal intensity is excluded from the parametric interaction in the strong coupling regime, which results in a twice-higher threshold.

The steady-state oscillations of the SRO with counterdirectional mode coupling above threshold were evaluated using coupled wave equations for the pump, signal, and idler waves in the plane wave approximation [16]. The equations were solved numerically to define the intracavity signal amplitude e_5^+ at the input end of the nonlinear crystal, which satisfies the loop equations (1), (5) for a given input pump intensity P_{in} and taking into account the minimum gain condition that follows from (8). If the unknown e_5^+ is found then the output pump (P_{out}) and idler (I_{out}) intensities follow from the coupled wave equations, while the SRO output intensity at the signal wavelength in forward and backward directions via mirrors 1 and 2 ($S_{\text{out1,2}}^{\pm}$) can be found using the loop equations.

Dependences of the SRO output parameters on the input pump in different regimes of counterdirectional mode coupling are compared in Fig. 8. Simulations were made for $R_1 = V = 1$ and $\alpha = 1 - R_2 = 10^{-2}$, and for different coupling constants $R_b = 0$, $R_b = 2.5 \times 10^{-5}$ ($\chi = 0.5$), $R_b = 4 \times 10^{-4}$ ($\chi = 2$). The SRO outputs are shown with respect to the input pump, while the horizontal scale is normalized to the SRO threshold (which is different for different coupling constants, see Fig. 7). As can be seen, normalized curves for the output pump and idler overlap in different regimes, although SRO thresholds in intermediate and strong coupling regimes are about 1.5 and 2 times higher than the threshold in the absence of coupling. Thus, the pump-to-idler conversion efficiency for the SRO with coun-
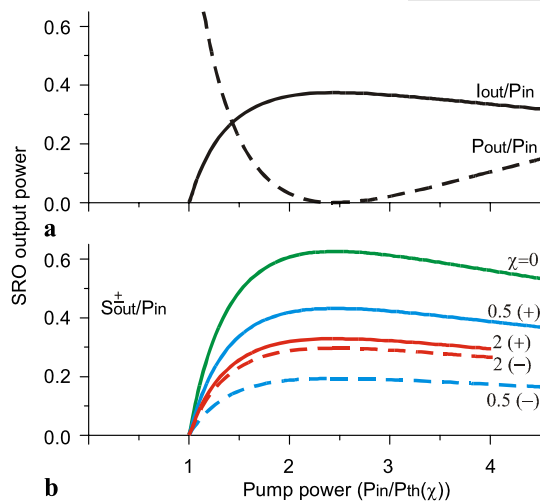
Fig. 8 SRO output at the pump, signal and idler wavelengths vs. input pump for different values of the parameter χ. The horizontal axis is normalized to the SRO threshold (which depends on χ). Vertical axes are normalized to the input pump. Part (**a**): the output idler (*solid curve*) and the output pump (*dashed curve*); curves for different values of the parameter χ are overlap. Part (**b**): the output signal in the forward (*solid curves*) and in the backward (*dashed curves*) directions

Fig. 9 SRO output at signal wavelength in forward and backward directions vs. parameter χ at different pump power levels. Vertical axes are normalized to the input pump. Part (**a**): the output signal in the forward direction. Part (**b**): the output signal in the backward direction

terdirectional mode coupling can be as high as for the SRO without coupling. However, it can be reached at higher pump power (twice higher in the strong coupling regime).

Due to the counterdirectional mode coupling the SRO output at signal wavelength occurs in two directions. The backward output intensity is smaller than the forward one in weak and intermediate regimes, whereas both intensities tend to be equal in the strong coupling regime. The dependence of the $S_{\mathrm{out}}^{-}/S_{\mathrm{out}}^{+}$ ratio on the parameter χ is shown in Fig. 7 by the dashed line (right vertical axis). As can be seen, the dependence is similar to that for the threshold but not exactly the same. The difference is due to the fact that the positions of the cavity transmission maxima in forward and backward directions do not coincide (see the section on the passive cavity). The formula for the $S_{\mathrm{out}}^{-}/S_{\mathrm{out}}^{+}$ ratio can be derived, without consideration of the parametric interaction. Hence, the parameter χ can be easily measured experimentally by measuring and comparing the SRO output power in two directions.

Figure 9 compares forward and backward SRO outputs as functions of the parameter χ. Simulations were made for different pump levels (shown with respect to the threshold of the SRO without coupling P_{th} ($\chi = 0$)). The SRO parameters are almost not affected in the weak coupling regime ($\chi < 0.1$) and the signal output is equally divided between forward and backward directions in the strong coupling regime ($\chi > 2$). The situation is more interesting in the intermediate regime. The SRO output in forward direction decreases with increasing parameter χ, and the SRO oscillations cease at some point if the pump power is low ($P_{\mathrm{in}} < 2 \times P_{\mathrm{th}}(0)$). On the other hand, the backward output
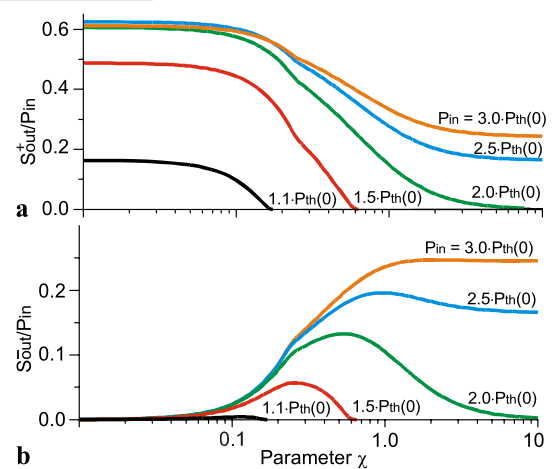
increases with an increase of the parameter χ and it passes through a maximum. Thus, a small variation of the coupling constant may cause a noticeable redistribution of the signal output between forward and backward directions. This feature can be used for active stabilization of the SRO as will be illustrated in the experimental section below.
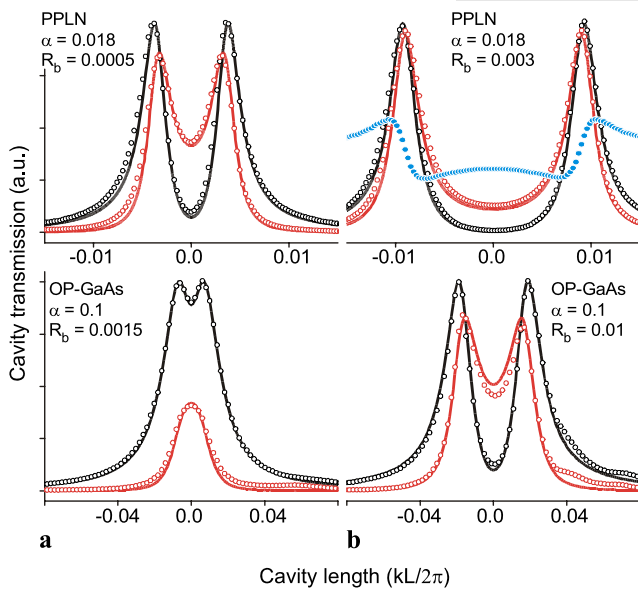
4 Experiments

4.1 Passive cavity

In the first experiments an external narrowband laser was resonantly coupled into the ring cavity with the QPM crystal. We used a standard bow-tie cavity arrangement with two plane and two curved mirrors. The temperature stabilized QPM crystal was located between curved mirrors in the waist of the cavity mode. Two types of QPM materials were characterized: (i) a commercial magnesium doped PPLN crystal (30 mm long, QPM periods about 30 μm), (ii) and a custom OP-GaAs crystal (12 mm long, QPM period of 58 μm). Both crystals were plane-parallel cut and AR/AR coated. A commercial laser with 1600 nm wavelength (Agilent 81642A) was used for experiments with the PPLN crystal. The OP-GaAs crystal was tested using a custom Tm- doped fiber laser at 1940 nm [11]. Experiments with the PPLN crystal were carried out using the cavity with highly reflective mirrors. The OP-GaAs crystal was characterized using the cavity with a 9% transmission input coupler.

Transmission resonances of the bow-tie ring cavity equipped with the PPLN and OP-GaAs crystals are shown in Fig. 10. The crystals were slightly tilted with respect to the optical axis of the cavity to avoid effects introduced by

Fig. 10 Transmission resonances of the passive cavity. *Top*: cavity with PPLN crystal, *bottom*: with OP-GaAs crystal. *Black* and *red hollow circles* show experimentally measured cavity transmission in forward and backward directions respectively; *solid lines* show the data fit by the model (see (2)); *blue circles* show obtained error signal

residual reflections of the AR coatings. A pair of identical and calibrated photodetectors was used to measure and compare the cavity transmissions in forward and backward directions. Resonance fringes of the cavity were observed at constant laser wavelength while the cavity length was scanned by a piezo.

Black and red hollow circles show the experimentally measured cavity transmission in forward and backward directions respectively. Solid curves show the cavity transmission calculated using (2). A standard data fitting technique was used in the latter case to determine the backward reflection parameter R_b and the cavity round-trip loss α.

There is a very good agreement between the experimental data and the simulation for the shape and for the relative height of forward and backward resonances. Hence, a ring cavity setup can be used as a precise tool for the measurement of weak backward reflections from optical materials.

The strength of the resonances splitting (and hence the value of the constant R_b) was found to be strongly dependent on the temperature of the crystal, the laser wavelength and the position of the cavity mode within the crystal, for both materials. Small changes of those parameters resulted in variation of R_b by orders of magnitude. For instance, part (a) of the figure shows the 'typical' strength of the splitting while part (b) shows the strongest splitting we observed. At certain temperatures of the crystals (or laser wavelengths) the parameter R_b was too small to cause the peak splitting. These observations are in good qualitative agreement with predictions of our model of back reflections in QPM material (see Sect. 2 and Fig. 2).

A small offset between the cavity transmission maxima in forward and backward direction has been used for active stabilization of the cavity with the PPLN crystal, as discussed in Sect. 3. The outputs of the two photodetectors were subtracted using a simple operational amplifier circuit to generate an error signal (shown in Fig. 10 by blue solid dots). The output of the subtractor was fed through a servo amplifier to the piezo, locking the cavity to the laser. The transmission of the locked cavity was fine tuned (maximized) by adjustment of the gain on the subtractor inputs. In this way the cavity was locked for extended periods of time, several hours.

Some discrepancies between the model and the experimental observations were revealed. The split resonances were not perfectly symmetric in frequency, as the model predicts (see (2)). The peak heights on the left- and on the right-hand of the split resonance were fluctuating in time (by a few percents). The asymmetry was more pronounced when the cavity was poorly aligned (or when the tilt of the QPM crystal with respect to the cavity axis was too strong). Moreover, our experiment is unable to verify whether the peak splitting is symmetric around the unperturbed resonance frequency of the cavity (in the absence of the counterdirectional mode coupling). Possibly, the observed asymmetry and variability of the split resonance can be explained and evaluated using more complex models.

4.2 Active cavity

In the next series of experiments, the bow-tie cavity with the PPLN crystal was tested in the active SRO regime. The crystal was pumped at 1064 nm using the 10 W output of an Yb-doped fiber amplifier (Keopsys KPS-YFA-40-SLM-PM) seeded by a single-frequency diode-pumped Nd:YAG laser (InnoLight Mephisto). Three of four cavity mirrors were HR (R > 99.9%) in the signal wavelength range of the SRO (1650–1850 nm) and HT (T > 95%) at pump and idler wavelengths. The fourth cavity mirror was the output coupler for the signal wave with ≈1% transmittance. The output coupler was replaced by another HR mirror in some experiments.

The round-trip losses of the SRO cavity were estimated using the specifications for the crystal's AR coatings and for the mirrors. Coupling constants $5 \times 10^{-4} \leq R_b \leq 3 \times 10^{-3}$ were measured, depending on the wavelength, the crystal temperature and position inside the QPM grating in experiments with the passive cavity (see Fig. 10). Thus, the strong coupling regime can be expected for the cavity equipped with all HR mirrors: $0.003 \leq \alpha \leq 0.009$, $2 \leq \chi \leq 15$, while the cavity with the partially transmissive output coupler should operate in the intermediate regime: $0.016 \leq \alpha \leq 0.024$, $1 \leq \chi \leq 3$.

Measured and estimated SRO thresholds are compared in Fig. 11. Measurements were carried out for both cavity
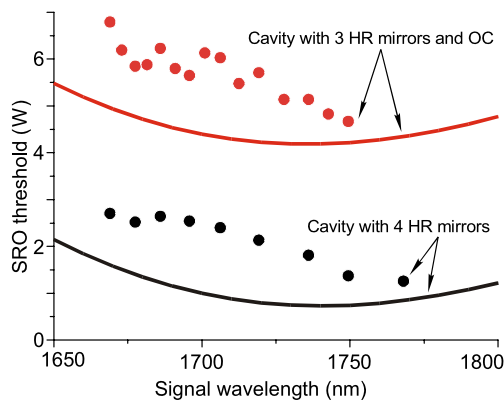
Fig. 11 SRO threshold vs. signal wavelength. *Circles* show experimentally measured values and *solid lines* show the theoretical estimates made for the SRO in the absence of the coupling. *Black color*: the bow-tie cavity with four HR mirrors. *Red color*: the cavity with three HR mirrors and 1% output coupler

Fig. 12 SRO outputs at signal wavelength vs. cavity length (piezo scanned) at different pump power levels. *Green curves* show the SRO output at signal wavelength in forward direction and *red curves* show the output in backward direction

arrangements in a range of signal wavelengths. Estimates were made for the SRO in the absence of the coupling, using the formula (7) for parametric interaction of optimally focused Gaussian beams. As can be seen, the measured thresholds are 1.7–2.7 times higher than estimates for the cavity with all HR mirrors (strong coupling regime), while the difference is about 1.2–1.4 times for the cavity equipped with the output coupler (intermediate regime). Thus, our experimental observations are in good agreement with predictions of the model, taking into account the uncertainties in evaluation of the coupling constant, the cavity losses and the approximate character of (7).

In the next experiment we simultaneously measured forward and backward SRO outputs at the signal wavelength by a pair of identical and calibrated photodetectors while the length of the cavity—and hence the signal wavelength—was scanned by a piezo. Waveforms acquired at different pump power are compared in Fig. 12. The time span in Fig. 10 corresponds to piezo scanning of the cavity by 0.5–1.0 FSR (SR = 0.9 GHz). The cavity was equipped with a 200 μm thick uncoated YAG etalon. The width of etalon transmission peak (180 GHz FWHM) is of the order of the parametric gain bandwidth (150 GHz FWHM). Hence the variation of the cavity loss and the gain over the cavity FSR is small (5×10^{-5}) and one can expect very weak and smooth dependence of the SRO output power on the cavity length. However, the experimentally observed forward output of piezo scanned SRO consists of series of well pronounced maxima (green lines in Fig. 12). If the pump power is close to the threshold (upper plot), the SRO oscillation ceases in some range of cavity lengths (signal wavelengths). With an increase of the pump power the SRO oscillates for any cavity length (lower plot). However, a strong variation of the signal output power occurs on a small scale with respect to the FSR of the cavity.
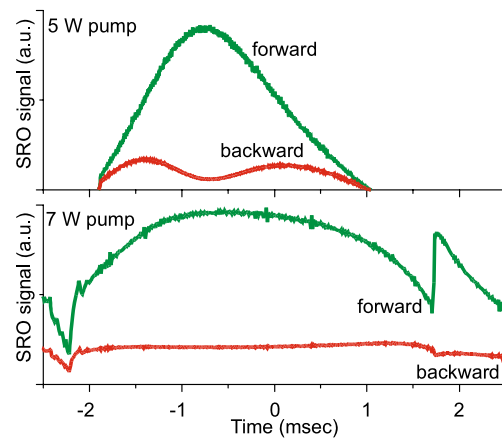
Our explanation for the observed variations of the SRO output is that they are due mostly to the coupling constant R_b (strongly wavelength dependent) rather than to the parametric gain and the etalon transmission (weakly wavelength dependent). As can be seen from Fig. 12 and in accordance with the model predictions (Fig. 9), the waveforms for forward and backward SRO outputs have different shape and the backward output passes through a minimum—more or less pronounced, depending on the pump power—when the forward output passes through a maximum.

We used this feature for active stabilization of the SRO cavity. Signals from the photodetectors were again sent to the subtractor circuit. The gains at the subtractor inputs were adjusted in such a way as to obtain a steep output signal vs. frequency with a zero crossing in vicinity to the maximum of the SRO output power. The output of the subtractor was fed through a servo amplifier to the piezo. In a sense, this method allows to lock the SRO cavity to the coupling constant R_b, which depends on the signal wavelength and on the crystal temperature. If the crystal's temperature is kept constant then the signal wavelength would be stabilized to the point where the R_b has a local minimum and hence the SRO output power in forward direction reaches the maximum.

The characteristics of the actively stabilized SRO are illustrated in Fig. 13 by green lines and compared with the parameters of the free-running SRO (red lines). The upper plot shows the SRO power at the signal wavelength and the lower plot shows the signal wavelength stability. The variations of the output power and the frequency of the actively stabilized SRO can be explained by the crystal's temperature fluctuations. Some adjustment of the subtractor's input gains was needed when the SRO was temperature-tuned in order to match the settings to the particular value of the coupling constant R_b.
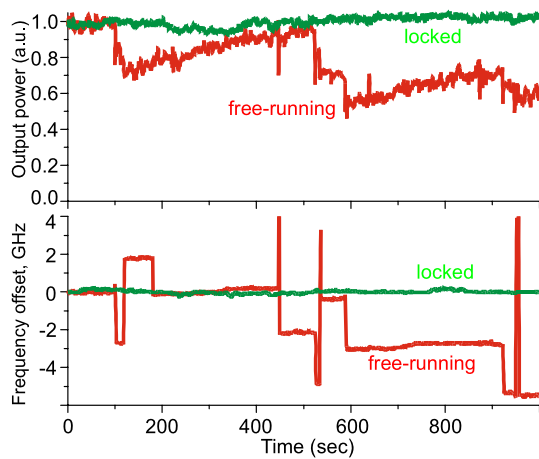
Fig. 13 SRO stability at signal wavelength. *Upper plot* shows the power stability and lower plot shows the frequency stability. *Red curves*: free-running SRO; *green curves*: actively stabilized SRO
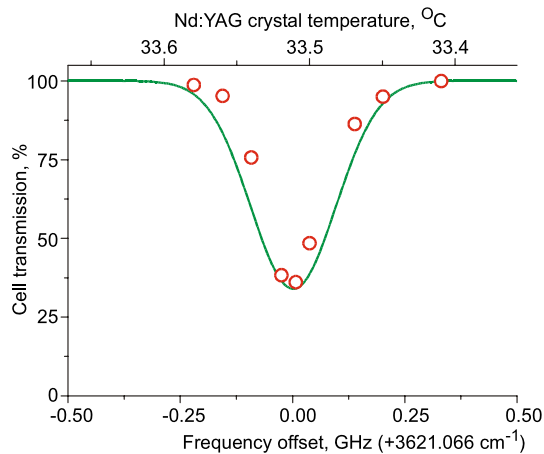
Fig. 14 CO_2 transition near 3621.066 cm^{-1}. 1-m long cell filled with CO_2 at 0.1 mbar. *Circles* show experimentally measured cell's transmission and *solid line* shows the simulation, based on data from HITRAN

The idler wavelength can be tuned by the pump wavelength tuning while the SRO cavity (and therefore the signal wavelength) is locked. We tested this tuning option by measuring a molecular (CO_2) gas absorption, as illustrated in Fig. 14. The 1-m long gas cell was filled with CO_2 at 0.1 mbar pressure. The SRO was coarse-tuned to the CO_2 transition by temperature tuning of the PPLN crystal and then the SRO cavity was locked. The idler was scanned through the absorption line by temperature tuning of the pump laser (tuning coefficient -3.24 ± 0.4 GHz/K). The temperature of the Nd:YAG crystal was adjusted manually, and the whole measurement took about 60 seconds. Figure 14 compares the experimentally measured cell transmission and a fit based on HITRAN data. The range of the continuous tuning of the idler was about 3 GHz (larger than shown in Fig. 14) and was limited by the mode hops of the

pump laser. A continuous tuning range of a few tens of GHz can be potentially obtained in this way, as the main limiting factor is the parametric gain bandwidth.

We also compared the present SRO stabilization with the usual approach, where the intracavity etalon is dithered and an error signal is obtained by demodulating the signal wave detector signal. No particular difference in the SRO's output characteristics was observed for the two lock methods.

5 Summary

We investigated the effects of counterdirectional mode coupling in ring resonators with QPM nonlinear crystals. Such resonators have two practical applications, enhancement of an external laser power e.g. for efficient nonlinear frequency mixing (second-harmonic, sum frequency, difference-frequency generation) or optical parametric oscillation.

We modeled back-reflection from QPM crystals (a cause of counterdirectional mode coupling) using simple simulations based on available data of the properties of OP-GaAs crystals. Our simulations show that the non-phase-matched back reflection may be rather high due to fluctuations of QPM grating parameters—2–3 orders of magnitude higher than that for the perfectly periodical structure. The simulations also predict a strong and irregular dependence of the back reflection on wavelength and on the QPM grating period.

Properties of a nominal ring cavity with counterdirectional mode coupling were evaluated by the use of loop equations in steady-state approximation. The system can be characterized by the parameter $\chi = \sqrt{R_b}/\alpha$ where R_b is the back reflection and α is the cavity round-trip loss. The root in the numerator indicates that even a weak back reflection (in comparison with other losses) can strongly alter the resonant properties of the cavity and hence must be taken into account in real applications.

In general, counterdirectional mode coupling can be considered as a parasitic effect. The coupling results in a decrease of the intracavity laser power that is usually the most important factor in applications where the cavity is used for enhancement of an external laser source. The maximum forward intracavity power can be a factor of 4 smaller than that in the absence of the coupling if χ exceeds unity. In an SRO application, the coupling may result in a threshold up to twice higher, although a pump conversion efficiency as high as in the absence of coupling can be reached if the pump power is sufficiently high. Another probable effect of the coupling is hopping of the signal frequency by few tens of MHz due to the cavity's resonance splitting.

The resonant properties of the ring cavity remain slightly different in two directions even in the strong coupling

regime ($\chi \gg 1$). The dissimilarity is a result of unidirectional excitation of the cavity by an external laser or of unidirectional amplification of the signal wave in the SRO. This feature can be used for active stabilization of the cavity. The cavity can be locked using a pair of photodetectors, a simple subtractor circuit and a standard servo amplifier. An advantage of the proposed stabilization technique is a combination of simplicity with a high speed (limited by time constants of the cavity). The main disadvantage of the method is the dependence of the shape of the generated error signal on the parameter R_b. However, this dependence is weak in the strong coupling regime.

The described effects of counterdirectional mode coupling were observed experimentally in ring cavities with a PPLN crystal and an OP-GaAs crystal. Back reflections in the range of 0.0005–0.003 and 0.0015–0.01, respectively, were measured for those materials. While residual back reflections and scattering on the AR coatings may be present, the strong dependence of the parameter R_b on laser wavelength, on the temperature of the crystal and on beam position within the crystal allowed us to associate a significant part of the measured back reflection with the QPM grating.

The measured shapes of the cavity resonances were in very good agreement with theoretical predictions, demonstrating that our ring cavity setup can be used as a precise tool for the measurement of weak backward reflections from optical materials. We locked the cavity with the PPLN crystal to a laser wave using the dissimilarity of cavity properties in opposite directions. This could be used for cavity-enhanced frequency conversion applications. Furthermore, we implemented the active stabilization of the SRO using a similar locking technique. The output power and the signal wavelength of the SRO were stabilized and the idler wavelength was fine-tunable by pump wavelength tuning.

We expect that the effects of the counterdirectional mode coupling could be suppressed by the use of an intracavity optical isolator. In this case the back reflection from the QPM crystal R_b will add to the cavity round-trip loss α. However, the advantage of restored directionality of the ring cavity does not necessarily outweigh unavoidable negative effects (e.g. additional losses on the isolator). Furthermore, the high intracavity laser power, which is essential for many practical applications, could lead to damage of the isolator.

Various effects due to back reflection can be expected in a standing wave cavity with a QPM crystal (e.g. etalon effects). Our model can be adapted to evaluate those effects. Instead of weak coupling between counterpropagating modes in the ring resonator one must consider a two-section standing wave resonator with a strong coupling between sections.

References

1. V.I. Sardyko, V.N. Severikov, J. Appl. Spectrosc. **26**, 592 (1977)
2. D.S. Weiss, V. Sandoghdar, J. Hare, V. Lefèvre-Seguin, J.-M. Raimond, S. Haroche, Opt. Lett. **20**, 1835 (1995)
3. B.E. Little, J.-P. Laine, S.T. Chu, Opt. Lett. **22**, 4 (1997)
4. M.L. Gorodetsky, A.D. Pryamikov, V.S. Ilchenko, J. Opt. Soc. Am. B **17**, 1051 (2000)
5. T.J. Kippenberg, S.M. Spillane, K.J. Vahala, Opt. Lett. **27**, 1669 (2002)
6. S. Götzinger, O. Benson, V. Sandoghdar, Opt. Lett. **27**, 80 (2002)
7. A. Mazzei, S. Götzinger, L.S. de Menezes, G. Zumofen, O. Benson, V. Sandoghdar, Phys. Rev. Lett. **99**, 173603 (2007)
8. Z. Zhang, M. Dainese, L. Wosinski, M. Qiu, Opt. Express **16**, 4621 (2008)
9. S. Vasilyev, S. Schiller, A. Nevsky, A. Grisard, D. Faye, E. Lallier, Z. Zhang, A.J. Boyland, J.K. Sahu, M. Ibsen, W.A. Clarkson, Opt. Lett. **33**, 1413 (2008)
10. O. Levi, T.J. Pinguet, T. Skauli, L.A. Eyres, K.R. Parameswaran, J.S. Harris Jr., M.M. Fejer, T.J. Kulp, S.E. Bisson, B. Gerard, E. Lallier, L. Becouarn, Opt. Lett. **27**, 2091 (2002)
11. S.E. Bisson, T.J. Kulp, O. Levi, J.S. Harris, M.M. Fejer, Appl. Phys. B **85**, 199 (2006)
12. L. Li, J. Opt. Soc. Am. A **10**, 2581 (1993)
13. S.V. Vasil'ev, V.A. Sychugov, Quantum Electron. **31**, 72 (2001)
14. D. Faye, A. Grisard, E. Lallier, B. Gérard, M. Avella, J. Jimenez, Appl. Phys. Lett. **93**, 151115 (2008)
15. B. Bendow, P.D. Gianino, Y.F. Tsay, S.S. Mitra, Appl. Opt. **13**, 2382 (1974)
16. M. Ebrahimzadeh, M.H. Dunn, *Optical Parametric Oscillators*. Handbook of Optics, vol. 4 (McGraw-Hill, New York, 1995). Chap. 22